ChemElectroChem

Research Article
doi.org/10.1002/celc.202500008

Chemistry Europe
European Chemical Societies Publishing

www.chemelectrochem.org

Biochar Cathodes for Bioelectrochemical Systems: Understanding the Effect of Material Heterogeneity on Performance for Abiotic Hydrogen Evolution Reaction

Shabnam Pouresmaeil, Thomas Schliermann, Matthias Schmidt, Falk Harnisch,* and Joerg Kretzschmar*

Granular carbon-based cathodes in carbon dioxide-reducing bioelectrochemical systems (CO_2-reducing BES) feature high biocompatibility and stability. Wood-based biochar is gaining popularity in (bio)electrochemical applications due to its sustainability and reduced environmental impact. Yet, previous studies primarily examined lab-scale biochars. This study investigates how heterogeneity of industrial-scale granular biochars (GBs) influences their electrocatalytic activity for hydrogen evolution reaction (HER) in the nexus of CO_2-reducing BES. Significant variations are identified in overpotentials for HER at $-1\,mA\,cm^{-2}$ ($\eta_{-1\,mA\,cm^{-2}}$) among the GB-based cathodes. Beechwood-derived GB pyrolyzed at 740 °C shows the lowest $\eta_{-1\,mA\,cm^{-2}}$ (223.6 ± 30.0 mV), outperforming birchwood-derived GB at 700 °C (503.5 ± 4.9 mV) and granular graphite (608.3 ± 19.5 mV). Despite its superior performance, beechwood-based GB shows high heterogeneity. Such heterogeneity underlies different physicochemical properties, likely due to uneven temperature distribution in industrial pyrolysis. The remarkable performance of beechwood-based GB pyrolyzed at 740 °C is attributed to its higher electrical conductivity, higher degree of carbonization, favorable H/C ratios, higher disorder in carbonaceous structure, and suitable porosity. The results highlight the influence of the wood type, the importance of systematic GB characterization, and the necessity to optimize industrial-scale biochar production to achieve homogeneous and high-performance biochar.

1. Introduction

Biochar is a carbon-rich material that is produced by pyrolysis from diverse biomasses, including, for instance, biowaste and wood.[1] Intrinsic features of biochar such as high porosity, mass-specific surface area (*mass-SSA*), fixed carbon, as well as electrical conductivity (σ) and pH led to its investigation for different areas of application, for example, enhancing soil fertility, immobilizing contaminants from gaseous phases, and treating wastewater.[2] Some specific properties of biochar such as high *mass-SSA* and good σ suggest its high suitability for developing biocompatible electrodes for bioelectrochemical systems (BES).[3–8] Special emphasis has been given to biocathodes in BES that reduce carbon dioxide (CO_2) to valuable products by using electroactive microorganisms (EAM). Among the products of these CO_2-reducing BES are mono- and multicarbon compounds such as methane,[9–12] acetic acid,[13,14] butyric acid,[15] and carboxylic acids.[16,17] The cathodic reduction of CO_2 by EAM is discussed to proceed either via direct electron transfer or indirectly, using hydrogen (H_2) as an electron

S. Pouresmaeil
Department of Biochemical Conversion
DBFZ Deutsches Biomasseforschungszentrum gemeinnützige GmbH
(German Biomass Research Center)
Torgauer Straße 116, 04347 Leipzig, Germany

T. Schliermann
Department of Thermochemical Conversion
DBFZ Deutsches Biomasseforschungszentrum gemeinnützige GmbH
(German Biomass Research Center)
Torgauer Straße 116, 04347 Leipzig, Germany

M. Schmidt
Department of Technical Biogeochemistry
UFZ-Helmholtz Centre for Environmental Research
Permoserstraße 15, 04318 Leipzig, Germany

F. Harnisch
Department of Microbial Biotechnology
UFZ-Helmholtz Centre for Environmental Research
Permoserstraße 15, 04318 Leipzig, Germany
E-mail: falk.harnisch@ufz.de

J. Kretzschmar
Faculty of Natural and Environmental Sciences
Zittau/Görlitz University of Applied Sciences
Theodor-Körner-Alle 16, 02763 Zittau, Germany
E-mail: Joerg.Kretzschmar@hszg.de

Supporting information for this article is available on the WWW under https://doi.org/10.1002/celc.202500008

carrier.[18,19] Recently, there has been a growing consensus that electron transfer takes place by in situ H_2 evolution reaction (HER) coupled to microbial H_2 utilization.[11,12,14,20,21]

In situ HER in CO_2-reducing BES is in advantage over ex situ supply of H_2 to microbial CO_2 fermentation systems as H_2 can be produced in direct vicinity of CO_2-reducing microorganisms. Furthermore, the rate of H_2 evolution can be adjusted to the microbial kinetics.[12,14] Both aspects can minimize the challenges that come with low H_2 solubility.

Cathode materials for CO_2-reducing BES need to possess low overpotential (η) for HER, high σ, high stability, and biocompatibility.[11,22,23] High volumetric-*SSA* can be achieved by using 3D electrodes, for instance, bed electrodes.[9,24–26] For bed electrodes, carbon-based cathodes such as granular activated carbon (GAC) and granular graphite (GG) are widely studied in CO_2-reducing BES.[9,10,27,28] Nonrenewable coal or petroleum are the precursors for the production of GAC. Furthermore, GG is mined or synthesized by thermal treatment of carbon-based material, thus contributing to greenhouse gas emissions.[3]

Commercial biochar production is an emerging carbon sequestration strategy, allowing waste valorization.[29] Biochar's capacity for carbon sequestration is about 0.56 kg CO_2 kg^{-1} biochar. Estimated carbon footprint is $\leq$0.08 kg CO_2 kg^{-1} biochar for granular biochar (GB) produced at 600–800 °C.[30] Total energy input for GB production at pyrolysis temperatures of 600 to 1000 °C, is one order of magnitude less than that of graphite production.[30] Therefore, GB cathodes derived at lower pyrolysis temperatures gain advantages in terms of sustainability and ecological advantages over graphite cathodes. Moreover, electrodes made from waste biomass suggest reducing investment and operating costs;[23,31] however, economic assessment was not the focus of this study. Performance of GB-based cathodes in CO_2-reducing BES has only been discussed in very few studies where biochar was produced by well-controlled pyrolysis on a lab scale.[8,30] Highest treatment temperature (HTT) in pyrolysis and the feedstock are the main factors affecting the physicochemical characteristics of biochar,[1,32] which was elaborated, for instance, on the σ of lab-scale wood-derived GB.[33,34] Biochar production on an industrial scale leads to heterogeneity within the product that may influence the quality and performance of the biochar across a specific application.[35] The desired characteristics of industrial-scale biochar for a specific application may therefore differ from lab-scale biochar, even when the same feedstock and HTT are used. These variations are crucial to be understood and subsequently limited when ultimately considering the suitability of industrial-scale biochar in future applications. To the best of our knowledge, there are no studies on how the heterogeneity-dependent characteristics of industrial-scale biochar contribute to the performance of GB-based cathodes in terms of HER for CO_2-reducing BES. We focus on the characterization of heterogeneous industrial-scale biochar to show its potential and current limitations for practical application as electrode material in BES.

Therefore, this study assesses the electrocatalytic activity for HER of cathodes based on two different industrial-scale GB produced from two different wood materials, i.e., beechwood as representative of a typical European hardwood and birchwood as a fast-growing softwood, both pyrolyzed at temperature of ≈700 °C. Furthermore, the study presents various parameters of the analyzed GB such as *mass-SSA*, microporosity, carbonization degree, σ, and carbonaceous structure while explaining how these factors may cause the observed diverse electrocatalytic activity for HER. This comprehensive characterization provides a profound insight needed for making informed choices about the future application of industrial-scale GB as a (bed) cathode, for example, for HER in CO_2-reducing BES.

2. Results and Discussion

2.1. Electrical Conductivity

The feedstock (i.e., type of wood) and operating parameters of pyrolysis such as heating rate, residence time, HTT, and granule size influence different structural characteristics and hence physical–chemical properties of biochar.[33,34,36] Therefore, it was expected to see differences in the electrical conductivity (σ) of GB from BEW740 and BIW700 arising mainly from their different feedstock. BIW700, made from birchwood, shows an average σ of 0.22 ± 0.09 S m^{-1} (**Table 1**). BEW740 made from beechwood shows more than two orders of magnitude higher average σ of 68.02 ± 74.64 S m^{-1}. This is in line with our expectations, as the higher σ of biochar from hardwood compared to softwood has already been shown.[34] Interestingly, σ measurements in GB of BEW740 showed high heterogeneity in σ. Thus, GB of BEW740 were sorted into classes 1 to 3 according to their σ. GB of BEW740-class1 shows the highest σ (162.50 ± 45 S m^{-1}) followed by BEW740-class 2 (41.55 ± 8.00 S m^{-1}) and BEW740-class3 (0.01 ± 0.04 S m^{-1}). Gabhi et al. measured σ of 229.20 S m^{-1} of monoliths of commercial hardwood-derived biochar by using a two-probe method at a contact pressure of 1 MPa,[33] which is in the order of magnitude of σ for BEW740-class1. The observed high heterogeneity of GB of BEW740 may derive from an uneven carbonization/pyrolysis temperature during the industrial pyrolysis process with lower maximum temperatures inside the GB bed. Therefore, GB derived from beechwood at 500 °C (BEW500) was studied. BEW500 and BEW740-class3 show marginal σ, emphasizing the hypothesis that not all granules of BEW740 were exposed to

Table 1. Electrical conductivity (σ) of biochar cubes along the growth direction of the wood.

Sample code	σ [S m^{-1}]	Sample size [n]
BIW700	0.22 ± 0.09	3
BEW740[a)]	68.02 ± 74.64	30
BEW740-class1	162.50 ± 45.00	10
BEW740-class2	41.55 ± 8.00	10
BEW740-class3	0.01 ± 0.04	10
BEW500	0.00	3
GG	37.40 ± 3.95	3

[a)]Bulk BEW740 without classification to class1-3.

the same maximum temperature of 740 °C since the degree of reproducibility of biochar production is strongly attributed to the level of control to ensure a uniform heat distribution inside the industrial pyrolysis reactor.[37] To understand the cause and impact of the heterogeneity in the σ of GB produced from a single type of wood in one pyrolysis batch, all three classes of BEW740 were used in all subsequent experiments in this study. GG as the control material exhibits a σ of 37.40 ± 3.95 S m^{-1}, consistent with earlier research on the electrical conductivity of bulk graphite, confirming the reliability of the measurements.[38]

2.2. Electrocatalytic Activity for Hydrogen Evolution Reaction of Single-Biochar Granules

2.2.1. Cyclic Voltammetry

Cyclic voltammetry (CV) analysis was used to assess the hydrogen evolution reaction (HER, Equation S1, Supporting Information) at GB and GG (control) under biologically relevant conditions (pH 7). The CV traces in **Figure 1**(a-b) represent the average of all forward and backward scans as well as the standard deviation among the different GB and GG samples. As expected, BIW700 cathodes exhibit low electrocatalytic activity for HER, reaching $j_{geom} = -1$ mA cm^{-2} only in two out of three measurements. CV analyses on 30 granules of BEW740 from all 3 classes show that j_{geom} varies from $\approx$0 mA cm^{-2} to over -7 mA cm^{-2} (Figure 1b), even though the tested GB were produced from the same type of wood in the same batch. BEW740-class1 shows the highest electrocatalytic activity among all GB samples (Figure 1a), whereas BEW740-class3 and BEW500 show no electrocatalytic activity for HER (Figure 1b). The very low electrocatalytic activity of BEW500 and BEW740-class3 shows that these cannot be used as cathodes for HER at all. GG shows a j_{geom} for HER that is comparable to BEW740-class1, but only at potentials more negative than -1.35 V, making BEW-740class1 the favorable electrode material for HER at less negative potentials and low rates in CO_2-reducing BES.

2.2.2. Overpotential for HER

Upon determining the onset potential (E_{onset}) of HER at -1 mA cm^{-2}, $\eta_{-1\ mA\ cm^{-2}}$ was calculated for BEW740-class1, BEW740-class2, BEW700, and GG cathodes which generated $j_{geom} \geq -1$ mA cm^{-2} (Figure 1c-d). As BEW740-class3 and BEW500 have no sufficient electrocatalytic activity for HER, $\eta_{-1\ mA\ cm^{-2}}$ was not calculated for them. HER commences at E_{onset} which is defined according to[39] as the intersection point of the extended tangent for HER with $j_{geom} = -1$ mA cm^{-2} and the potential axis, which is shifted to $j_{geom} = 0.0$ mA cm^{-2} (Figure S4, Supporting Information). The lowest $\eta_{-1\ mA\ cm^{-2}}$ was observed in BEW740-class1 (223.6 ± 30.0 mV). Remarkably, GG exhibited the highest $\eta_{-1\ mA\ cm^{-2}}$ (608.3 ± 19.5 mV), followed by BIW700 (503.5 ± 4.9 mV) and BEW740-class2. $\eta_{-1\ mA\ cm^{-2}}$ is in good agreement with j_{geom} generated by BEW740-class1, BIW700, and GG (Figure 1a). Current generation by GG also reaches >-1 mA cm^{-2} but at more negative potentials, resulting in higher $\eta_{-1\ mA\ cm^{-2}}$ compared to BEW740-class1. BEW740-class2 exhibits $\eta_{-1\ mA\ cm^{-2}}$ of 449.5 ± 69.7 mV, which is twice as high as that of BEW740-class1, being consistent with the observed j_{geom} in CV (Figure 1b). The best and worst performing GB in

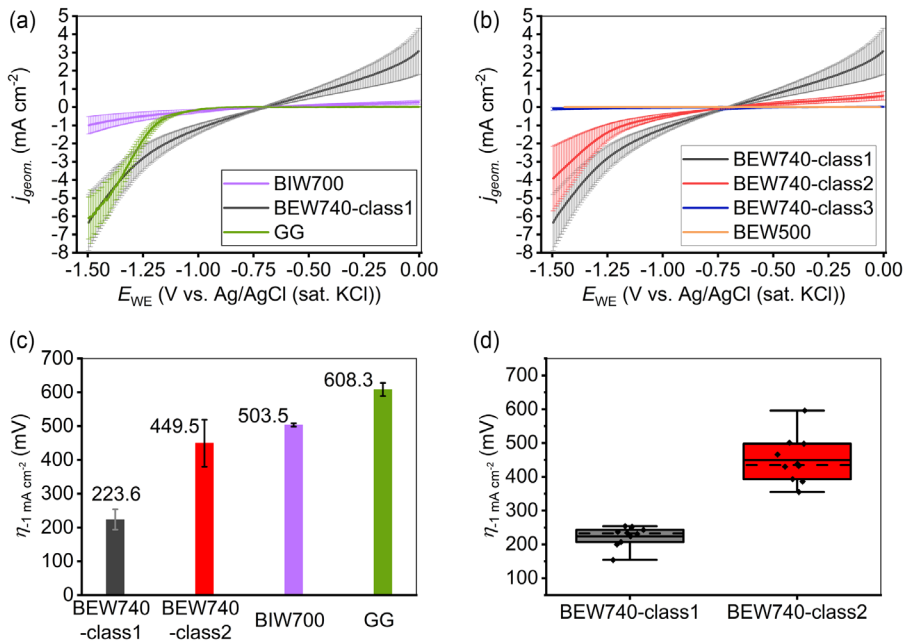

Figure 1. Electrochemical characteristics of GB granules and GG: a) CV data adapted from cyclic voltammograms for BEW740-class1 ($n = 10$), BIW700 ($n = 3$), and GG ($n = 3$); and b) CV data adapted from cyclic voltammograms for three classes of BWE-740 ($n = 10$ for each class) and BEW500 ($n = 3$); c) overpotential for HER at $j_{geom} = -1$ mA cm^{-2} ($\eta_{-1\ mA\ cm^{-2}}$) with GB-based cathodes of BEW740-class1 ($n = 10$), BEW740-class 2 ($n = 10$), BIW700 ($n = 3$), and GG ($n = 3$); d) box plot and distributions of $\eta_{-1\ mA\ cm^{-2}}$ for BEW 740-class1 and class2; dashed line and solid line refer to median and mean values, respectively. Error bars indicate standard deviation.

terms of $\eta_{-1\ mA\ cm^{-2}}$ for HER depict a good correlation between cathode performance and σ.

$\eta_{-1\ mA\ cm^{-2}}$ for BEW740-class1 and -class2 remained lower than the control (GG), indicating that GB from both classes are superior electrocatalysts for HER at $j_{geom} = -1\ mA\ cm^{-2}$. Therefore, BEW740-class1 and class2 were further analyzed. In Figure 1d, a thorough comparison between BEW740-class1 and BEW740-class2 reveals that the probability distribution of $\eta_{-1\ mA\ cm^{-2}}$ for HER with BEW740-class1 is narrower and slightly left-skewed, whereas BEW740-class2 shows a right-skewed distribution. However, there is no clear violation from normality. In summary, BEW740-class1 and -class2 are the most suitable cathodes, but their $\eta_{-1\ mA\ cm^{-2}}$ for HER are significantly different. This result exemplifies the heterogeneity of industrial-based biochar with regard to its suitability to serve as cathode material in the example of HER. This underlines the importance of a systematic evaluation of cathodes based on biochar and other pyrolyzed renewable materials. Based on these findings, we conducted a systematic investigation into the physicochemical properties potentially influencing the electrocatalytic activity of biochar cathodes produced by industrial pyrolysis. This shall establish a foundation for characterizing and utilizing renewable GB-based cathodes in future applications.

2.2.3. Degree of Carbonization and Carbonaceous Structure

In pyrolysis, wood degrades into amorphous black carbon (a-C) and/or hydrogenated amorphous carbon (a-C:H). The degree of carbonization is defined as the measured carbon content in biochar. a-C and a-C:H have sp^2 electron configurations and therefore show semiconductor-like behavior.[34] **Figure 2** shows the elemental carbon content of the GB. The carbon content of BEW740-class1 and -class2 is 92.83 ± 0.47 wt% and 92.80 ± 0.17 wt%, respectively, with only slight differences between them. BIW700 has a carbon content of 92.13 ± 0.20 wt%. Carbon content of BEW740-class3 (92.26 ± 0.20 wt%) was higher than that of BEW500 (91.60 ± 0.39 wt%); however, all the samples show a narrow range of elemental carbon content, suggesting that the degree of carbonization reaches a plateau, and further temperature increase does not affect it within this temperature range (500–740 °C). Laterally resolved energy-dispersive X-ray spectroscopy (EDX) mapping of BEW740-class1 and -class3 revealed a homogeneous distribution of carbon on the surface, supporting the uniformity of carbon composition across the samples. As expected, GG consists of about 99.40 wt% elemental carbon (H content was not measured). Despite the minor differences in the carbon content of GB samples, their σ varies by several orders of magnitude (see Table 1). In the carbonization process, when carbon content reaches 90.00 wt%, a slight increase in carbon content potentially results in a sharp decrease in H content.[34] Hydrogen content increased from 0.55 ± 0.04 wt% (BEW740-class1) to 0.80 ± 0.02 wt% (BEW740-class2) and finally to 1.56 ± 0.04 wt% (BEW740-class3). It is also noteworthy that BEW500, BEW740-class3, and BIW700 have the highest H content, which is expected from their carbon content. In carbonization, chemically bound atoms of H and O are driven out. H and O atoms avoid the formation of sp^2 and sp^3 clusters, whereas sp^2 electron configuration is essential for electron conduction in carbon structures.[40] Therefore, the ratio of H/C should be monitored in addition to the degree of carbonization.[33] Figure 2 displays H/C atomic ratio for all GB. It is evident that the H/C atomic ratio of BEW740-class1 (0.07 ± 0.01) is much lower than that of BEW740-class3 (0.20 ± 0.01), with BEW740-class2 having an intermediate ratio (0.10 ± 0.00). These results suggest that the carbonization of BEW740 did not occur uniformly, resulting in varying σ and significantly different electrocatalytic activities for HER. BEW500, BEW740-class3, and BIW700 have the highest H/C atomic ratio of 0.28 ± 0.00, 0.20 ± 0.06, and 0.19 ± 0.02, respectively. Gabhi et al. reported a similar H/C (≈0.11) for the most electrically conductive biochar pyrolyzed on a laboratory scale at 1000 °C.[34]

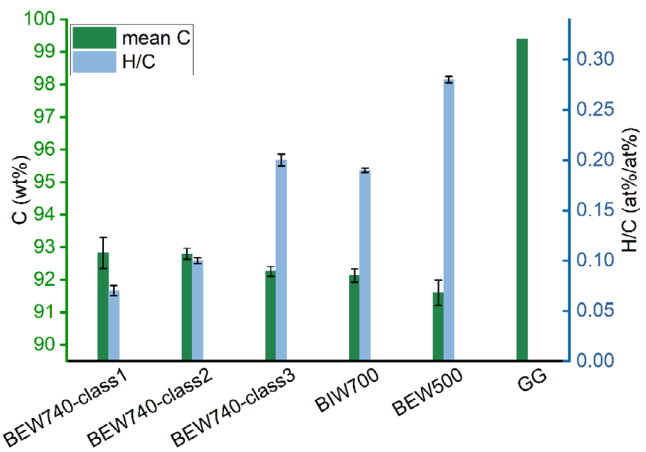

Figure 2. Carbon content of each type of GBs (n = 3) and GG, control, (n = 1) (green, left Y-axis) and H/C atomic ratio (blue, right Y-axis). Error bars indicate standard deviation.

Additionally, thermogravimetric analysis coupled with mass spectrometry (TGA-MS) was carried out to assess the mass loss and relevant volatile compounds of the GB samples as a function of temperature in the range of 100–800 °C. BIW700, BEW740-class1 and -class2 underwent the highest mass loss at a temperature below 110 °C (Figure S5, Supporting Information) mainly because of water loss at the same temperature range (Figures S6a-b, Supporting Information). Almost no H_2 and minimum CO evolved from BEW740-class1 and -class2 (Figures S6c-d, Supporting Information). BEW740-class3 and BEW500 lost a big fraction of weight at ≈600 and 700 °C (Figure S5, Supporting Information), mainly resulting from H_2 and CO evolution (Figures S6c-d, Supporting Information). CO_2 was evolved from all the GB samples (Figure S6e, Supporting Information), and the maximum amounts were detected for BEW740-class3 and BEW500. Although BEW740 is a biochar produced at 740 °C, some granules possess identical properties to BEW500, proving again evidence that not all of the wood granules have been carbonized homogeneously. The results of TGA and TGA-MS confirm the results of elemental analysis, showing that BEW740-class1 has the most complete carbonization in this study. Better carbonization of biomass promotes devolatilization, which increases the degree of carbonization and enrichment of inorganic components, including transition metals.[41] Inductively coupled plasma optical emission (ICP-OES) and EDX analyses of BEW740-class1 and -class3 confirmed trace amounts of Fe and Cu in both

samples, with higher concentrations in BEW740-class1 (Figure S7-8, and Table S1, Supporting Information). The lower overpotential of fully carbonized BEW740-class1 may very unlikely stem from its very slightly increased content of catalytically active transition metals; in contrast, the only minimal surface metal signals (EDX) and trace bulk metal concentrations (ICP-OES) suggest that the observed HER activity is primarily due to the carbon matrix and its electrical conductivity.

X-ray photoelectron spectroscopy (XPS) analysis reveals key differences in surface chemistry that explain the contrasting electrochemical behavior of BEW740-class1 and -class3. The corresponding XPS spectra are presented in Figure S9a-b. Atomic concentration of each peak is shown in Table S2, Supporting Information. BEW740-class1, which showed the lowest overpotential for HER, exhibited a higher surface carbon content (72.3 at.%) with 61.6 at.% C—C compared to BEW740-class3, which contains only 64.4 at.% surface carbon content with 51.0 at.% C—C carbon. This result supports a greater degree of carbonization in BEW740-class1. In the C1s spectrum, BEW740-class1 was dominated by a peak at 285.0 eV (C—C), which is attributed to the presence of surface sp^2 carbon, suggesting a partially graphitized and conductive carbon matrix.[42] In contrast, BEW740-class3 displayed additional peaks at 286.7 and 288.9 eV, which can be assigned to C—O and O—C═O functional groups,[43] respectively, indicating a more oxygenated and less conductive carbon surface. Although nitrogen was detected only in class3 (0.3 at.%), likely as pyrrolic group in aromatics,[43] its low content cannot influence HER performance. Critically, class3 shows some contamination with transition metals (1.5 at.% Fe, 0.8 at.% Cr) that are completely absent in -class1. The O1s spectra further confirm this, with BEW740-class3 displaying the insulating metal oxides (Fe_2O_3, Cr_2O_3) peak at 529.85 eV[44] and higher overall oxygen content (26.5% vs 24.0%), indicating incomplete carbonization and surface oxidation that may not allow creating a fully conductive carbon network. The XPS results agree with the electrochemical data, supporting that BEW740-class1 benefits from a more carbon-rich, less functionalized, and electronically conductive surface, which underpins its enhanced HER performance.

Microstructure of GB was assessed with Raman microspectroscopy to evaluate the state and distribution of sp^2-bonded carbon.[45] The Raman spectra of all GB and GG are shown in **Figure 3**. They were analyzed by fitting the Lorentzian/Gaussian peak functions after the subtraction of the photoluminescence contribution to study regions of interest, that is, the G-band and D-band (Figure S10, Supporting Information). These bands can provide information on the carbon microstructure.[45–48] G-band at 1575 cm^{-1} and D-band at 1357 cm^{-1} result from crystallite[46] and disordered graphitic structure,[32] respectively. Biochar has a disordered structure; therefore, the G- and D-bands exhibit the amorphous structure with small aromatic rings and the condensed structure with large aromatic rings, respectively.[49] The lateral size of crystalline carbon clusters (L_a) of the polyaromatic unit was shown to be directly proportional to the square root of the integrated area of the D-band to G-band ($(I_D/I_G)^{0.5}$) for disordered structure.[45,50–52] L_a can be estimated directly from I_D/I_G by using Ferrari–Robertson equation,[52] where the excitation-dependent ((C′) is corrected (≈0.0063).[53] **Table 2** represents the intensity ratio of (I_D/I_G), L_a, peak position (w), and sharpness of the peaks based on the full width of the peak (Δw) for GB and GG. Among the GB, the highest I_D/I_G (2.18 ± 0.08) was achieved for BEW740-class1, which has the most complete carbonization and the least $\eta_{-1\ mA\ cm^{-2}}$.

I_D/I_G ratio increases as the pyrolysis temperature increases.[34] Higher temperature in the carbonization process results in more depolymerization, causing the formation of isolated sp^2 carbon atoms[54] and/or a decrease in the sp^3 content in a-C.[34] Gabhi et al. demonstrated that I_D/I_G increases with the size of graphite nanocrystallites, indicating a transformation from a-C to nanocrystalline graphite.[34] Furthermore, the highly disordered crystalline clusters, which consist of 3–4 turbostratically stacked layers with average L_a up to 30 Å, can be regarded as highly disordered graphitic lattices.[55] Results in Table 2 suggest that BEW740-class1 exhibits the biggest L_a, which supports its best-disordered structure

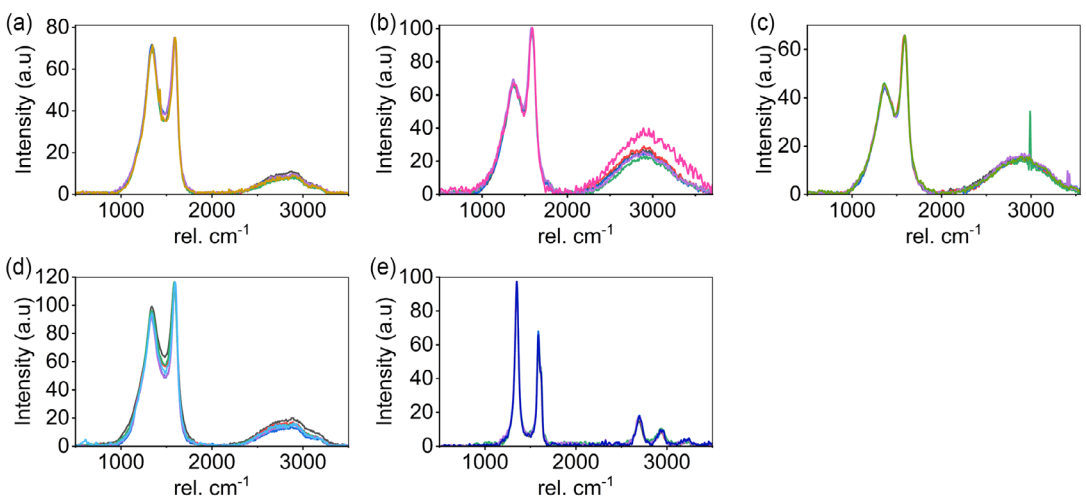

Figure 3. Raman spectra (n = 6) on: a) BEW740-class1; b) BEW740-class3; c) BEW500; d) BIW700; and e) GG.

Table 2. Intensity ratios (I_D/I_G), lateral size of crystalline carbon clusters (L_a), position of D-, G-, and 2D- band(s) (w_D, w_G, and w_{2D}), and the full width of the peak (Δw) in the half-maximum peak value GB and GG. All data are the average of data from $n = 6$ spectra on each sample. The uncertainties of the measurements/analyses are given as standard deviation.

Material	I_D/I_G	L_a [Å]	w_D [cm^{-1}]	w_G [cm^{-1}]	W_{2D} [cm^{-1}]	Δw_D	Δw_G	Δw_{2D}
BIW700	2.14 ± 0.14	18.4 ± 4.7	1335 ± 4	1590 ± 4	2825 ± 27	207 ± 11	78 ± 9	508 ± 20
BEW740-class1	2.18 ± 0.08	18.6 ± 2.5	1341 ± 3	1591 ± 2	2800 ± 1	175 ± 7	75 ± 3	500 ± 1
BEW740-class3	1.72 ± 0.11	16.5 ± 4.2	1365 ± 6	1585 ± 3	2898 ± 27	284 ± 10	109 ± 5	678 ± 65
BEW500	1.62 ± 0.07	16.0 ± 3.3	1361 ± 4	1588 ± 2	2871 ± 13	252 ± 11	106 ± 5	595 ± 23
GG	1.83 ± 0.71	17.0 ± 10.6	1350 ± 1	1585 ± 2	2698 ± 5	49 ± 1	37 ± 6	83 ± 7

with turbostratic arrangement. An even more comprehensive assessment of structural ordering would require additional analyses using transmission electron microscopy and X-ray diffraction. G-band appeared on all the spectra obtained from GB and was centered in the range from 1585 ± 3 to 1591 ± 2 cm^{-1}. A conspicuous difference in the D-band position was observed for the studied GB, ranging from 1335 ± 4 to 1365 ± 6 cm^{-1}. BIW700 and BEW740-class1 showed a lower D-band position than BEW500 and BEW740-class3, consistent with findings by Amdani and Oginni et al.[49,54] which demonstrated a decrease in biochar D-band position with higher carbonization temperatures. The GG spectrum shows G-, D-, and 2D-bands at 1585 ± 2, 1350 ± 1, and 2698 ± 5 cm^{-1}, respectively, aligning with values reported for pristine natural graphite powder.[56]

Scanning helium ion microscopy (HIM), a high-resolution microscopy technique, is known to provide a charge contrast on top of the structural information of the sample surface. The charge contrast renders non/poorly electrically conductive areas darker due to the increased surface barrier that the secondary electrons have to overcome in order to be detected.[57] This is reflected in **Figure 4** where the nonconductive BEW740-class3 shows several black spots, presumably tarry substances which are not observed on the conductive BEW740-class1.

2.2.4. Surface Area and Microporosity

Detailed pore structural characteristics were determined from N_2 adsorption–desorption isotherms at 77 K (Figure S11, Supporting Information) and are presented in **Table 3**. BEW740-class1, the most promising GB in terms of $\eta_{\text{-1 mA cm}^{-2}}$ for HER, had the highest *mass-SSA* (307.6 ± 79.5 m^2 g^{-1}). Although the *mass-SSA* of BEW740-class3 decreased to 22.2 ± 6.2 m^2 g^{-1}, having a higher surface area does not necessarily ensure the best electrochemical performance for a biochar. For example, even though BEW500 had a *mass-SSA* of 267.5 ± 85.1 m^2 g^{-1}, it exhibited poor performance as a cathode for HER, similar to BEW740-class3. The pyrolysis temperature between 500 and ≈700 °C may not affect *mass-SSA*, which is consistent with results reported by Mochidzuki et al.[58] Among all GB, BEW740-class1 has the highest $V_{0.97}$ and V_{DR}, with 0.19 ± 0.03 and 0.115 ± 0.035 cm^3 g^{-1}, respectively. Crucially, this sample also exhibited the highest σ, suggesting that morphology is the combined effect of accessible porosity and electrical conductivity that can influence HER efficiency. In the samples from BEW740-class3, $V_{0.97}$ decreased to 0.02 ± 0.01 cm^3 g^{-1}, and V_{DR} dropped to 0.003 ± 0.001 cm^3 g^{-1}. V_{DR} in BEW500 is 0.048 ± 0.018 cm^3 g^{-1}, while $V_{0.97}$ is relatively high, 0.15 ± 0.01 cm^3 g^{-1}. Although BEW740-class3 and BEW500 have

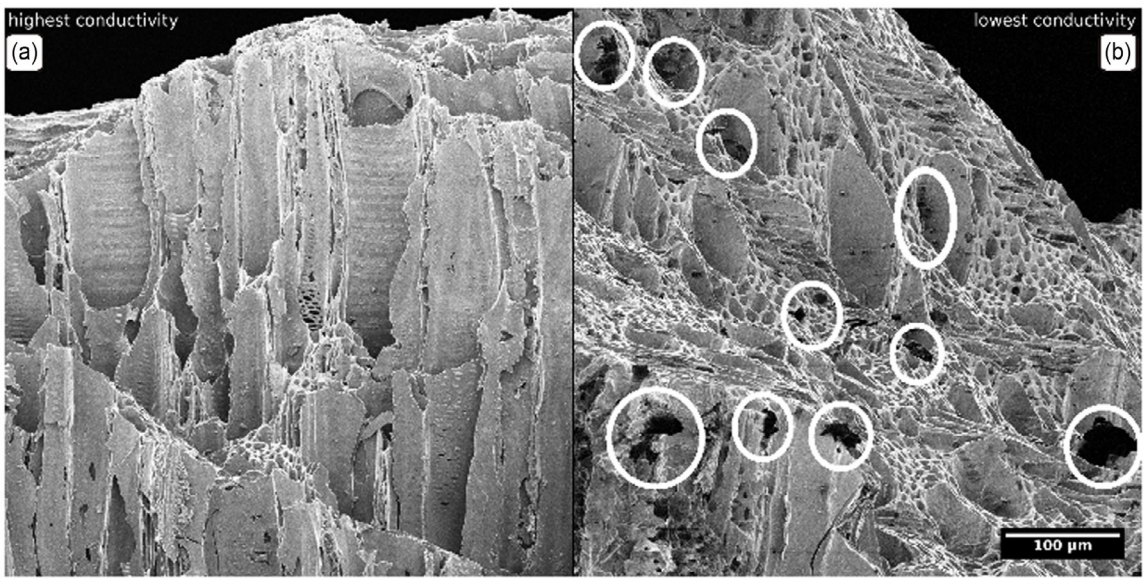

Figure 4. Helium ion microscopy (HIM) images of BEW740: a) BEW-class1; b) BEW740-class3. No charge compensation was used for imaging, resulting in black spots appearing on poorly conductive samples (examples indicated by white circles).

Table 3. Porous characteristics of GB and GG including specific surface area based on Brunauer–Emmett–Teller method (*mass-SSA*), total available volume for N_2 through the adsorption isotherm at relative nitrogen pressure of 0.97 ($V_{0.97}$), micropore volume based on Dubinin–Radushkevich method (V_{DR}), and relevant micropores' width. All data represent the mean value for each type of GB ($n = 3$). Standard deviation is used to show the uncertainty of measurement.

Material	*mass-SSA* [$m^2\ g^{-1}$]	$V_{0.97}$ [$cm^3\ g^{-1}$]	V_{DR} [$cm^3\ g^{-1}$]	Micropore width [nm]
BIW700	188.8 ± 24.6	0.09 ± 0.01	0.063 ± 0.025	1.28 ± 0.06
BEW740-class1	307.6 ± 79.5	0.19 ± 0.03	0.115 ± 0.035	1.14 ± 0.05
BEW740-class2	272.4 ± 58.8	0.13 ± 0.02	0.088 ± 0.024	1.12 ± 0.09
BEW740-class3	22.2 ± 6.2	0.02 ± 0.01	0.003 ± 0.001	ND[a)]
BEW500	267.5 ± 85.1	0.15 ± 0.01	0.048 ± 0.018	1.28 ± 0.10
GG	0.8 ± 0.2	0.004 ± 0.001	0.000	ND[1]

[a)]Micropore width is not determined (ND) for BEW740-class3 and GG since their micropore volume is approximately zero.

different *mass-SSA*, lower V_{DR} is more obvious for them. Comparable performance of BEW500 and BEW740-class3 in terms of poor σ and $j_{geom.}$ suggests that while *mass-SSA* contributes to the available surface for electrocatalytic activity, the proportion of electrochemically accessible micropores and the electrode's ability to transport charge are equally critical. Biochar electrodes with higher micropore volume, in addition to high mass-SSA, are likely to increase the electroactive sites and potentially facilitate proton accumulation through increased electric double-layer formation. This is especially important at neutral pH condition, where proton concentration is low. However, without sufficient σ, the benefit of high *mass-SSA* and microporosity cannot be recognized because sluggish charge transfer becomes the limiting step.

3. Conclusions

We show that GB obtained from an industrial pyrolysis process within one batch does substantially vary in terms of its physicochemical properties and thus also its electrocatalytic activity for HER. The heterogeneity is assumed to result from an uneven temperature distribution during the industrial pyrolysis process.

Specifically, we identified GB made from beechwood at 740 °C (BEW740-class1 and -class2) as the most suitable among all the tested GB to serve as cathodes for HER, with BEW740-class1 having the lowest overpotential. This is due to higher electrical conductivity, a greater degree of carbonization and thus lower H/C ratios, increased disorder in the carbonaceous structure, and suitable porosity. In contrast, GB originating from birchwood (BIW700) exhibited higher overpotentials, highlighting the influence of feedstock on the electrocatalytic activity of GB-based cathodes besides the pyrolysis temperature.

Our findings underline the importance of optimizing biochar production processes toward homogeneity of the gained GB to enhance the consistency and performance of GB-based cathodes. This basic understanding shall guide future research and development in the application of biochar-based materials in sustainable BES, particularly in CO_2-reducing BES supplied by in situ HER. For instance, future work should focus on refining the pyrolysis conditions and feedstock selection to achieve more uniform and high-performance biochar, indicated by the degree of carbonization, microporosity volume, disorder in carbonaceous structure, and electrical conductivity. Additionally, electrochemical characterization of the single granules of biochar cathode does not allow for revealing technological bottlenecks for the implementation of industrial GB in future BES. Therefore, exploring GB in different architectures of laboratory-scale reactors based on fixed/fluidized bed electrodes will be a key area of future investigation to optimize hydrodynamic properties and resistance (potential distribution) by designing a specific reactor configuration and operational control.

4. Experimental Section

Chemicals, Reference Electrodes, Biochar Granules

All chemicals were of at least analytical grade and supplied by Carl Roth GmbH (Karlsruhe, Germany) or Merck KGaA (Darmstadt, Germany). Deionized water (Millipore, Darmstadt, Germany) was used for preparing all solutions. All provided electrochemical potentials referred to Ag/AgCl sat. KCl reference electrodes (RE, +197 mV vs. standard hydrogen electrode (SHE)). All biochar samples were commercially available and were supplied by LUCRAT GmbH (Steinfurt, Germany). Biochar was produced by pyrolysis at different temperatures using beechwood and birchwood (see **Table 4** for details). Each biochar was sieved to gain biochar particles in a defined size range of 3–5 mm (Retsch AS300, Retsch GmbH, Haan, Germany). Graphite granules (enViro-cell Umwelttechnik GmbH, Oberursel, Germany) were used as control material.

Electrical Conductivity

Electrical conductivity (σ) of the biochar was measured by the two-probe method at room temperature (≈20 °C). GB and GG particles were slightly polished using sandpaper (grit P220, VSM Vereinigte

Table 4. General information on different GB and GG.

Sample ID	Wood type	HTT [°C]	Size range[a)] [mm]
BIW700	Birchwood	700	5–8
BEW740[b)]	Beechwood	740	5–8
BEW500	Beechwood	500	5–8
GG	Graphite Granules (control)	–	5–6

[a)]The size refers to the smallest length-dimension of a granule. [b)]In this study, the experimental results of σ were used to classify BEW740 biochar samples/cathodes into three groups of BEW740-class1, -class2, and -class3 (for details, see results and discussion).

Schmirgel und Maschinen-Fabriken AG, Germany) to prepare a cube-like particle for σ measurements. Details of the measurement setup are shown in Figure S1, Supporting Information. σ is calculated as follows.

$$\sigma = L/R.A \quad (1)$$

where R is the measured resistance in Ω, A is the cross-sectional area of a cube-like particle in cm^2, and L is the distance between the electrodes in mm (measured by using a caliper). All dimensions were converted to m prior to use in Equation (1).

Electrochemical Setup and Electrode Preparation

All electrochemical experiments were carried out in two-chamber reactors using a three-electrode setup based on three-neck round-bottom flasks with a working volume of 250 mL (Figure S2a, Supporting Information). The anode chamber was a 50 mL tailor-made glass tube (working volume of 20 mL) inserted into the three-neck round-bottom flask and ionically connected to the cathode chamber via a cation exchange membrane (fumasepFKE, FuMA-Tech GmbH, Germany) fixed by an O-ring and an aluminum cap. Anodes (counter electrodes, CE) were made of graphite rods ($d = 10$ mm, $L = 20$ mm, $A = 7.1$ cm^2, quality CP-2200, CP-Graphitprodukte GmbH, Germany). The graphite rods were connected to a current collector made of stainless-steel wire ($d = 0.5$ mm, Goodfellow GmbH, Germany) inserted into the graphite rod and fixed using epoxy glue (Toolcraft, Conrad Electronic SE, Germany). The current collector was isolated with a shrink tube made of modified polyolefin (ABB Ltd., Switzerland) and fixed to the electrode with epoxy glue. Cathodes (working electrodes, WE) were made of a GB connected to a current collector made of titanium ($d = 0.5$ mm, Goodfellow GmbH, Germany) using the same procedure as described for the anodes. The cathodic current collector was isolated with a glass capillary ($d = 1.0$ mm). For control measurements, the GG-based cathodes (control) were prepared as described for the GB-based cathodes. The RE (SE11, Xylem Analytics Germany Sales GmbH & Co. KG Sensortechnik Meinsberg, Germany) was positioned in the cathode chamber and fixed with a chloroprene stopper (Deutsch & Neumann GmbH, Germany). About 50 mM phosphate buffer (pH ≈7.0) was used as electrolyte solution (i.e., anolyte and catholyte). The catholyte solution was purged with nitrogen gas (N_2 5.0, Linde AG, Germany) for 25 min prior to all experiments and during all experiments to remove dissolved oxygen and avoid an increase in hydrogen partial pressure. Gas outlets were made of hollow needles pierced through the stoppers and connected to Tygon tubes immersed into a water lock. The electrochemical reactors were placed into an incubator hood (Unihood 650, UniEquip, Germany) at a 35 °C to mimic mesophilic condition in CO_2-reducing BES. During the experiments, the electrolyte solution in the electrochemical reactor was stirred at 150 rpm by using a magnetic stirrer (Variomag Poly 15, Thermo Scientific, USA).

Electrochemical Characterization

All experiments were performed by using a multipotentiostat (PARSTAT MC equipped with PMC-1000 cards, AMETEK Inc., USA). CV was applied at a scan rate of 1 mV s^{-1} in a potential range of 0.0 to −1.5 V. The third cycle was used for data analysis.[59] Control tests were conducted using the GG-based cathodes in an identical setup and operating conditions. Current data were normalized to the geometric surface area of the WE, resulting in geometric current density ($j_{geom.}$, mA cm^{-2}). For the GB-based cathodes, a cube was assumed, and individual maximum length dimensions were measured three times with a caliper (Figure S2b, Supporting Information). The GG-based cathode was assumed to be a sphere, and its diameter was measured with a caliper three times. CV results were used to determine the overpotential (η) for the HER at a fixed current density[39] in order to qualitatively explore the differences in the electrocatalytic activity of GB- and GG-based cathodes, explained SI, Equation S1–6, Supporting Information. As the highest $j_{geom.}$ at CO_2-reducing BES was reported at −1 mA cm^{-2},[12] η was calculated at $j_{geom.}$ of −1 mA cm^{-2} ($\eta_{-1\ mA\ cm^{-2}}$).

Physicochemical Characterization of GG and GB

Elemental composition and carbonaceous structure: A Vario MacroCube elemental analysis system (Elementar, Langenselbold, Germany) was used to determine the carbon (C), hydrogen (H), and nitrogen (N) composition of the samples. The measurement was conducted in accordance with DIN EN ISO 16948 standards (additional explanation in SI). To estimate the results in terms of dry matter (TS), the water content of a subsample was measured with a Karl Fischer titration method (Ti-Touch, Metrohm, Herisau, Switzerland).

TGA-MS was conducted as a supplementary for elemental analysis to qualitatively monitor carbon, hydrogen, and oxygen compounds in the form of water (H_2O), hydrogen molecule (H_2), carbon dioxide (CO_2), and carbon monoxide (CO), evolved from GB samples when heating up from 100 to 800 °C at 20 °C min^{-1}. TGA-MS was performed with NETZSCH STA 449 F3 Jupiter (NETZSCH GmbH & Co. Germany), with additional explanation in SI.

Spatially resolved element mapping was carried out by energy-dispersive X-ray spectroscopy (EDX) using a Zeiss Merlin VP Compact scanning electron microscope (Carl Zeiss Microscopy, Oberkochen, Germany) equipped with a Bruker Quantax XFlash Flat Quad detector (Bruker Nano Analytics, Berlin, Germany); additional explanation in SI. Bulk content of transition metals in biochar samples was measured using ICP-OES (iCAP6300, Thermo Fisher Science, USA), with additional explanation in SI. XPS was performed to analyze the elemental composition on the surface of biochar samples (XPS Kratos Ultra DLD). A detailed explanation of the method is available in the SI. The degree of disorder in the carbonaceous structure of GBs and graphite was determined from Raman microspectroscopy using a WITec Alpha 300RA (WITec Wissenschaftliche Instrumente und Technologie GmbH, Ulm, Germany), equipped with 532 nm excitation wavelength at a laser power of 2.5 mW (additional explanation in SI). Raman spectra were recorded at various positions on the sample within a spectrum range of 500–3500 cm^{-1}.

The surface topographies of the so-prepared GB and GG samples were studied with a Zeiss Orion NanoFab scanning helium ion microscope (Carl Zeiss Microscopy, Peabody, MA, USA), with additional explanation in SI. In order to obtain overview maps for navigation on the sample, several 800 × 800 μm^2 fields of view were stitched together using the ImageJ plug-in by Preibisch et al.[60]

Porous Characteristics

A fully automated volumetric sorption analyzer (3P micro 200, 3P Instruments GmbH & Co. KG, Germany) was used to record N_2 adsorption–desorption isotherms at −196.15 °C. All the samples were degassed for 120 min at 150 °C prior to the analysis using the integrated turbo pump. The sample weight was measured after degassing to normalize the data based on the weight of sample. The isotherms were measured with a combined approach. For relative pressures (p/p^0) <0.001, the adsorption branch was measured with the fixed-dose method (doses of 2 mL g^{-1}), resulting in p/p^0 for each measurement point depending on the adsorption behavior of the respective sample. For $p/p^0 > 0.001$, the pressure table method was used with predefined relative pressures for both adsorption and desorption branches. Using this procedure, the p/p^0 range of $<10^{-6}$ (depending on the microporosity of the sample) up to ≈1 could be measured, allowing for the detection of micro- and mesopores. Upon each dosing of the sample for $p/p^0 < 10^{-3}$, the process was allowed to equilibrate for 30 min, taking into account slow

adsorption into narrow micropores at −196.15 °C. Brunauer–Emmett–Teller (BET) was used to determine the *mass-SSA* from a limited linear region of the adsorption isotherm,[61] when the p/p^0 range was selected by ASiQwin software based on the algorithm taking into account the Rouquerol criteria.[62] Micropore volume (V_{DR}) was evaluated by applying Dubinin–Radushkevich (DR) equation on N_2 adsorption isotherms.[63] The characteristic size of the micropores was estimated from DR equation using a relation between the characteristic energy of adsorption and the micropore width.[64] The total available volume for N_2 through the adsorption isotherm was determined at relative nitrogen pressure of 0.97 ($V_{0.97}$).[65] Data analysis was performed on ASiQwin software (version 5.0, 1994-2016, Quantachrome Instruments).

Statistical Analysis

The CV profiles, $\eta_{\text{-1 mA cm}^{-2}}$, σ, elemental composition, volatile compounds, SA_{BET}, $V_{0.97}$, and V_{DR} resulted from measurements on three different granules of BEW500, BIW700, and GG ($n = 3$). For BEW740, the CV profiles, $\eta_{\text{-1 mA cm}^{-2}}$, and σ were conducted on 30 granules, 10 from each class ($n = 10$). Standard deviation on the datasets was calculated to report uncertainties of measurements. To assess the differences between BEW740-class1 and -class2 (see Table 1) in terms of $\eta_{\text{-1 mA cm}^{-2}}$, analyses were performed by two-sample *t*-test at the 0.05 level on the respective data. Data were processed using Origin software Version 9.9.0.225 (Origin 2022, OriginLab Corporation, Northampton, MA, USA).

Acknowledgements

The authors thank the ProVIS Centre for Chemical Microscopy, which was supported by European Regional Development Funds (EFRE), and the Helmholtz Association for using their microanalytical facilities. The authors greatly acknowledge Jan Griebel from Leibniz Institute of Surface Engineering (IOM), Leipzig, for XPS measurements.

Conflict of Interest

The authors declare no conflict of interest.

Data Availability Statement

The data that support the findings of this study are available from the corresponding author upon reasonable request.

Keywords: biochar · cathode · heterogeneity · overpotential · physiochemical characterization

[1] A. Shaaban, S.-M. Se, N. M. M. Mitan, M. F. Dimin, *Proc. Eng.* **2013**, *68*, 365.
[2] F. R. Amin, Y. Huang, Y. He, R. Zhang, G. Liu, C. Chen, *Clean Techn. Environ. Policy* **2016**, *18*, 1457.
[3] T. Huggins, H. Wang, J. Kearns, P. Jenkins, Z. J. Ren, *Biores. Technol.* **2014**, *157*, 114.
[4] Y. Yuan, T. Yuan, D. Wang, J. Tang, S. Zhou, *Biores. Technol.* **2013**, *144*, 115.
[5] M. Li, H. Zhang, T. Xiao, S. Wang, B. Zhang, D. Chen, M. Su, J. Tang, *Electrochim. Acta* **2018**, *283*, 780.
[6] K. Zhong, M. Li, Y. Yang, H. Zhang, B. Zhang, J. Tang, J. Yan, M. Su, Z. Yang, *Appl. Energy* **2019**, *242*, 516.
[7] K. Tahir, W. Miran, J. Jang, N. Maile, A. Shahzad, M. Moztahida, A. A. Ghani, B. Kim, H. Jeon, D. S. Lee, *Sci. Total Environ.* **2021**, *773*, 145677.
[8] G. Ghiara, S. Campisi, A. Goglio, F. Formicola, M. Balordi, A. Gervasini, S. Trasatti, F. Adani, A. Franzetti, P. Cristiani, *Sustain Energy Technol. Assess.* **2023**, *57*, 103274.
[9] P. Clauwaert, W. Verstraete, *Appl. Microbiol. Biotechnol.* **2009**, *82*, 829.
[10] D. Liu, M. Roca-Puigros, F. Geppert, L. Caizán-Juanarena, S. P. Na Ayudthaya, C. Buisman, A. Ter Heijne, *Front. Bioeng. Biotechnol.* **2018**, *6*, 78.
[11] F. Kracke, A. B. Wong, K. Maegaard, J. S. Deutzmann, M. A. Hubert, C. Hahn, T. F. Jaramillo, A. M. Spormann, *Commun. Chem.* **2019**, *2*.
[12] F. Kracke, J. S. Deutzmann, W. Gu, A. M. Spormann, *Green Chem.* **2020**, *22*, 6194.
[13] K. P. Nevin, S. A. Hensley, A. E. Franks, Z. M. Summers, J. Ou, T. L. Woodard, O. L. Snoeyenbos-West, D. R. Lovley, *Appl. Environ. Microbiol.* **2011**, *77*, 2882.
[14] J. S. Deutzmann, A. M. Spormann, *Biores. Technol. Rep.* **2024**, *25*, 101740.
[15] R. Ganigué, S. Puig, P. Batlle-Vilanova, M. D. Balaguer, J. Colprim, *Chem. Commun.* **2015**, *51*, 3235.
[16] J. B. Arends, S. A. Patil, H. Roume, K. Rabaey, *J. CO2 Util.* **2017**, *20*, 141.
[17] I. Vassilev, P. A. Hernandez, P. Batlle-Vilanova, S. Freguia, J. O. Krömer, J. Keller, P. Ledezma, B. Virdis, *ACS Sustainable Chem. Eng.* **2018**, *6*, 8485.
[18] M. C. A. A. van Eerten-Jansen, N. C. Jansen, C. M. Plugge, V. de Wilde, C. J. N. Buisman, A. Ter Heijne, *J. Chem. Technol. Biotechnol.* **2015**, *90*, 963.
[19] S. Cheng, D. Xing, D. F. Call, B. E. Logan, *Environ. Sci. Technol* **2009**, *43*, 3953.
[20] S. Bajracharya, S. Srikanth, G. Mohanakrishna, R. Zacharia, D. P. Strik, D. Pant, *J. Power Sources* **2017**, *356*, 256.
[21] F. Kracke, J. S. Deutzmann, B. S. Jayathilake, S. H. Pang, S. Chandrasekaran, S. E. Baker, A. M. Spormann, *Front. Microbiol.* **2021**, *12*, 696473.
[22] F. Geppert, D. Liu, M. van Eerten-Jansen, E. Weidner, C. Buisman, A. Ter Heijne, *Trends Biotechnol.* **2016**, *34*, 879.
[23] Y. Zhang, I. Angelidaki, *Environ. Sci. Technol* **2016**, *50*, 5432.
[24] S. Freguia, K. Rabaey, Z. Yuan, J. Keller, *Electrochim. Acta* **2007**, *53*, 598.
[25] J. R. Quejigo, B. Korth, A. Kuchenbuch, F. Harnisch, *ChemSusChem* **2021**, *14*, 1155.
[26] J. Rodrigo Quejigo, S. Tejedor-Sanz, A. Esteve-Núñez, F. Harnisch, *ChemTexts* **2019**, *5*.
[27] M. Brandão Lavender, S. Pang, D. Liu, L. Jourdin, A. Ter Heijne, *Biores. Technol.* **2022**, *347*, 126650.
[28] L. Caizán-Juanarena, T. Sleutels, M. Kokko, R. Berenguer, A. t. Heijne, *Emerging Trends And Advances In Microbial Electrochemical Technologies : Hypothesis, Design, Operation, and Applications*, Elsevier, NY **2024**, 425–478.
[29] D. Matovic, *Energy* **2011**, *36*, 2011.
[30] S. Antic Gorrazzi, D. Massazza, A. Pedetta, L. Silva, B. Prados, G. Fouga, S. Bonanni, *RSC Sustain.* **2023**, *1*, 1200.
[31] W. Yang, S. Chen, *Ind. Eng. Chem. Res.* **2020**, *59*, 6391.
[32] L. Zhao, X. Cao, O. Mašek, A. Zimmerman, *J. Hazard Mater.* **2013**, *256–257*, 1.
[33] R. S. Gabhi, D. W. Kirk, C. Q. Jia, *Carbon* **2017**, *116*, 435.
[34] R. Gabhi, L. Basile, D. W. Kirk, M. Giorcelli, A. Tagliaferro, C. Q. Jia, *Biochar* **2020**, *2*, 369.
[35] T. D. Bucheli, H. J. Bachmann, F. Blum, D. Bürge, R. Giger, I. Hilber, J. Keita, J. Leifeld, H.-P. Schmidt, *J. Anal. Appl. Pyrolysis* **2014**, *107*, 25.
[36] Y. Chen, S. S. A. Syed-Hassan, Q. Li, Z. Deng, X. Hu, J. Xu, L. Jiang, S. Su, S. Hu, Y. Wang, J. Xiang, *Fuel Process. Technol.* **2022**, *235*, 107366.
[37] O. Mašek, W. Buss, A. Roy-Poirier, W. Lowe, C. Peters, P. Brownsort, D. Mignard, C. Pritchard, S. Sohi, *J. Anal. Appl. Pyrolysis* **2018**, *132*, 200.
[38] S. Rattanaweeranon, P. Limsuwan, V. Thongpool, V. Piriyawong, P. Asanithi, *Proc. Eng.* **2012**, *32*, 1100.
[39] S. Wirth, F. Harnisch, M. Weinmann, U. Schröder, *Appl. Catal B Environ.* **2012**, *126*, 225.
[40] D. Dasgupta, F. Demichelis, A. Tagliaferro, *Philos. Mag. B* **1991**, *63*, 1255.
[41] T. Lu, H. Yuan, Y. Wang, H. Huang, Y. Chen, *J. Mater. Cycles Waste Manag.* **2016**, *18*, 725.
[42] Y. Lin, Z. Feng, L. Yu, Q. Gu, S. Wu, D. S. Su, *Chem. Commun.* **2017**, *53*, 4834.
[43] M. Ayiania, M. Smith, A. J. Hensley, L. Scudiero, J.-S. McEwen, M. Garcia-Perez, *Carbon* **2020**, *162*, 528.
[44] E Paparazzo, *J. Electron Spectrosc. Relat. Phenom.* **1987**, *43*, 97.
[45] Y.-R. Rhim, D. Zhang, D. H. Fairbrother, K. A. Wepasnick, K. J. Livi, R. J. Bodnar, D. C. Nagle, *Carbon* **2010**, *48*, 1012.
[46] A Cuesta, P Dhamelincourt, J Laureyns, *Carbon* **1994**, *32*, 1523.
[47] T. Gruber, W. Zerda, M. Gerspacher, *Carbon* **1994**, *32*, 1377.

[48] K. Ishimaru, T. Hata, P. Bronsveld, T. Nishizawa, Y. Imamura, *J. Wood Sci.* **2007**, *53*, 442.
[49] R. Z. Amdani, *Raman Spectroscopy for Characterizing Porous Carbon Material, M.Sc. thesis* , Lund University, Lund, Sweden **2020**.
[50] N. Larouche, B. L. Stansfield, *Carbon* **2010**, *48*, 620.
[51] F. Tuinstra, J. L. Koenig, *J. Chem. Phys.* **1969**, *53*, 1126.
[52] A. C. Ferrari, J. Robertson, *Phys. Rev. B* **2000**, *61*, 14095.
[53] K. C. Le, T. Pino, T. van Pham, J. Henriksson, S. Török, P.-E. Bengtsson, *Combust. Flame* **2019**, *209*, 291.
[54] O. Oginni, K. Singh, *J. Environ. Chem. Eng.* **2020**, *8*, 104169.
[55] A. Sadezky, H. Muckenhuber, H. Grothe, R. Niessner, U. Pöschl, *Carbon* **2005**, *43*, 1731.
[56] L. Guardia, M. J. Fernández-Merino, J. I. Paredes, P. Solís-Fernández, S. Villar-Rodil, A. Martínez-Alonso, J. Tascón, *Carbon* **2011**, *49*, 1653.
[57] M. Schmidt, J. M. Byrne, I. J. Maasilta, *Beilstein J. Nanotechnol.* **2021**, *12*, 1.
[58] K. Mochidzuki, F. Soutric, K. Tadokoro, M. J. Antal, M. Tóth, B. Zelei, G. Várhegyi, *Ind. Eng. Chem. Res.* **2003**, *42*, 5140.
[59] J. Rodrigo Quejigo, L. F. Rosa, F. Harnisch, *Electrochem. Commun.* **2018**, *90*, 78.
[60] S. Preibisch, S. Saalfeld, P. Tomancak, *Bioinformatics* **2009**, *25*, 1463.
[61] P. Webb, C. Orr, Micromeritics Instrument Corporation, *Analytical Methods In Fine Particle Technology*, Micromeritics Instrument Corp., Norcross, Ga. **1997**.
[62] F. Rouquerol, J. Rouquerol, K. Sing, P. Llewellyn, G. Maurin, *Adsorption By Powders And Porous Solids: Principles, Methodology And Applications*, 2nd ed., Academics Press, Oxford **2014**.
[63] M. M. Dubinin, *Chem. Rev.* **1960**, *60*, 235.
[64] M. M. Dubinin, H. F. Stoeckli, *J. Colloid Interface Sci.* **1980**, *75*, 34.
[65] J. Jagiello, J. Kenvin, A. Celzard, V. Fierro, *Carbon* **2019**, *144*, 206.

Manuscript received: January 13, 2025
Revised manuscript received: June 5, 2025
Version of record online: